Undergraduate honors thesis:
The shape of optimal convection cells

Matthew LeDuc
Department of Physics, University of Michigan

Under the direction of David Goluskin[1,3] and Charles Doering[1,2,3]
1. Department of Mathematics, University of Michigan
2. Department of Physics, University of Michigan
3. Center for the Study of Complex Systems, University of Michigan

1 Introduction

Over 100 years ago the French physicist Henri Bénard was inspired by the accidental discovery of cellular convection, and so for his doctoral dissertation he performed experiments on thin differentially heated layers of fluid. He observed many phenomena that we now recognize as characteristic of the convection that partially bears his name, including that it only occurred after a critical temperature had been reached and that the convection occurred in a cellular pattern with heat rising in the middle of the cell and falling at the edges. Sixteen years later, Lord Rayleigh used the Boussinesq equations – a modification of the incompressible Navier–Stokes equations that account for buoyancy – to create a theoretical framework for Bénard's obervations, and so the theory of Rayleigh–Bénard convection was born. His model relied on differential buoyancy forces created by temperature gradients in the fluid, and it predicted that sufficiently destabilizing temperature gradients would drive fluid motion.

Rayleigh's work was a seminal development in the theory of convection, but it turned out to not be the explanation of Bénard's observations. Rayleigh's model relies on the existence of a temperature gradient in the fluid to cause buoyancy forces, which is indeed the mechanism that typically drives convection in nature, but was not what caused the convection cells seen in Bénard's experiments. In 1958, J. R. A. Pearson, a researcher employed by a paint company, showed that under the conditions of Bénard's original experiments, convection was primarily driven by temperature-dependent surface tension rather than temperature-dependent buoyancy [5]. Pearson developed his theory of surface tension-driven instability after observing circulation in paint regardless of the orientation of its free surface, while Rayleigh's model required the free surface to be oriented opposite the direction of gravity.

Even though Rayleigh's model does not explain Bénard's observations, Rayleigh–Bénard convection and the Boussinesq equations have found widespread application in fields such as oceanography, atmospheric science, astrophysics, and engineering. Furthermore, in modern nonlinear science, the Rayleigh–Bénard model has become one of the most popular systems for studying pattern formation, spatiotemporal chaos, and turbulence.

In the present work, we investigate the heat transport ability of Rayleigh–Bénard convection in two dimensions with free-slip boundaries when optimizing the aspect ratio of the convection cells. This heat transport is typically quantified by the dimensionless Nusselt number Nu, which is the ratio of total heat transport to conductive heat transport. Of particular interest is the dependence of Nu on the Rayleigh number, Ra, which is a dimensionless parameter proportional to the temperature difference between the top and bottom of the domain. In the 2D free-slip configuration, it has been proven mathematically that Nu can grow no faster than $Ra^{5/12}$ as $Ra \to \infty$ [6]. However, for steady convection cells in a fixed domain, Nu grows at the slower rate

of $Ra^{1/3}$ [3]. The object of the present work is to determine whether steady convection cells can produce faster growth of Nu if the geometry of the convection cells is chosen to maximize Nu. The optimal choice of geometry will generally depend on Ra and on another dimensionless control parameter, the Prandtl number Pr. In the case of steady 2D convection with no-slip boundaries, it has been reported that optimizing the geometry of the convection cells indeed raises the rate at which Nu grows with Ra, raising the scaling exponent from 0.28 in the nonoptimized case to 0.31 in the optimized case [2].

2 The Boussinesq equations

We consider a two-dimensional domain of height $0 \le z \le h$ and length $0 \le x \le L$. We nondimensionalize lengths using the height h, which gives a domain $[0, \Gamma) \times [0, 1]$, where $\Gamma = \frac{L}{h}$ is the aspect ratio of the domain. We nondimensionalize time using the timescale of thermal diffusion. In dimensionless form, the Boussinesq equations governing Rayleigh–Bénard convection consist of the continuity equation

$$\nabla \cdot \mathbf{u} = 0, \tag{1}$$

the momentum equation

$$\partial_t \mathbf{u} + (\mathbf{u} \cdot \nabla)\mathbf{u} = -\nabla p + Pr\nabla^2 \mathbf{u} + PrRaT\mathbf{k}, \tag{2}$$

and the temperature equation

$$\partial_t T + (\mathbf{u} \cdot \nabla)T = \nabla^2 T, \tag{3}$$

where T is the temperature and $\mathbf{u} = u\ \mathbf{i} + w\ \mathbf{k}$ is the fluid velocity. The Rayleigh and Prandtl numbers are defined as

$$Ra = \frac{g\alpha h^3 \Delta}{\kappa\nu}, \qquad\qquad Pr = \frac{\nu}{\kappa}, \tag{4}$$

where g is the acceleration due to gravity, α is the coefficient of thermal expansion, Δ is the temperature difference from the bottom to top layers of fluid, ν is the kinematic viscosity, and κ is the thermal diffusivity.

The stream function Ψ is defined so that it is related to the vorticity ω by

$$\omega = -\nabla^2 \Psi = \partial_z u - \partial_x w. \tag{5}$$

The velocity components are related to the stream function by $u = -\partial_z \Psi$ and $w = \partial_x \Psi$. We can rewrite the temperature equation in terms of the stream function using the identities

$$(\mathbf{u} \cdot \nabla)T = u\partial_x T + w\partial_z T, \tag{6}$$

$$\partial_t T - \partial_z \Psi \partial_x T + \partial_x \Psi \partial_z T = \nabla^2 T, \tag{7}$$

$$-\partial_z \Psi \partial_x T + \partial_x \Psi \partial_z T = \begin{vmatrix} \partial_x \Psi & \partial_z \Psi \\ \partial_x T & \partial_z T \end{vmatrix} = \{\Psi, T\}. \tag{8}$$

Using this, the temperature equation can be written as

$$\partial_t T + \{\Psi, T\} = \nabla^2 T. \tag{9}$$

The momentum equation (2) is a vector equation. Writing the equations for u and w separately gives

$$\partial_t u + (\mathbf{u}\cdot\nabla)u = -\partial_x p + Pr\nabla^2 u, \tag{10}$$

$$\partial_t w + (\mathbf{u}\cdot\nabla)w = -\partial_z p + Pr\nabla^2 w + PrRaT. \tag{11}$$

To find an equation for $\omega = -\nabla^2\Psi$, we take $\partial_z(10) - \partial_x(11)$ to find

$$\partial_t\omega + \partial_z((u\partial_x u) + w\partial_z u) - \partial_x(u\partial_x w + w\partial_z w) = Pr\nabla^2\omega - PrRa\partial_x T. \tag{12}$$

Expanding all derivatives gives

$$\partial_z u\partial_x u + u\partial_{xz}u + \partial_z w\partial_z u + w\partial_{zz}u - (\partial_x u\partial_x w + u\partial_{xx}w + \partial_x w\partial_z w + w\partial_{xz}w = Pr\nabla^2\omega - PrRa\partial_x T. \tag{13}$$

Since $u = -\partial_z\Psi$ and $w = \partial_x\Psi$, $\partial_x u = -\partial_z w$, we can rewrite the left side of (13) as

$$u(\partial_{xz}u - \partial_{xx}w) + w(\partial_{zz}u - \partial_{xz}w) = u\partial_x(\partial_z u - \partial_x w) + w\partial_z(\partial_z u - \partial_x w). \tag{14}$$

Recalling that $u = -\partial_z\Psi$ and $w = \partial_x\Psi$, we find that this is equivalent to $-\partial_z\Psi\partial_x\omega + \partial_x\Psi\partial_z\omega = \{\Psi,\omega\}$. So, the momentum equation can be written in terms of Ψ and ω as

$$\partial_t\omega + \{\Psi,\omega\} = Pr\nabla^2\omega - PrRa\partial_x T. \tag{15}$$

In summary, the stream function formulation of the 2D Boussinesq equations is

$$\partial_t T + \{\Psi, T\} = \nabla^2 T, \tag{16}$$

$$\partial_t\omega + \{\Psi,\omega\} = Pr\nabla^2\omega - PrRa\partial_x T. \tag{17}$$

When solving the Boussinesq equations numerically, it is convenient to rescale the domain from $0 \le x \le \Gamma$ to $0 \le x' \le 2\pi$ and from $0 \le z \le 1$ to $-1 \le z' \le 1$, so we use the transformation

$$x' = \frac{2\pi}{\Gamma}x, \quad z' = 2z - 1. \tag{18}$$

The derivatives ∂_z and ∂_x then transform as

$$\partial_{x'} = \frac{\Gamma}{2\pi}\partial_x, \quad \partial_{z'} = \frac{1}{2}\partial_z. \tag{19}$$

With this transformation, the Boussinesq equations become

$$\partial_t T + \frac{4\pi}{\Gamma}\{\Psi, T\} = \nabla'^2 T, \tag{20}$$

$$\partial_t\omega + \frac{4\pi}{\Gamma}\{\Psi,\omega\} = Pr\nabla'^2\omega - PrRa\frac{2\pi}{\Gamma}\partial_x T, \tag{21}$$

where $\nabla'^2 = \partial_x^2 + \partial_z^2 = (\frac{2\pi}{\Gamma})^2\partial_{x'}^2 + 4\partial_{z'}^2$.

In order to make computations simpler, we write $T(x,z) = T_0(z) + \Theta(x,z)$, where the base linear temperature profile $T_0(z)$ is given by

$$T_0(z) = -z. \tag{22}$$

Noting that $\partial_x T_0(z) = 0$ and $\partial_z T_0(z) = -1$ and substituting for $T(x,z)$, we can rewrite (20)–(21) as

$$\partial_t\Theta + \frac{4\pi}{\Gamma}(\{\Psi,\Theta\} - \partial_x\Psi) = \nabla'^2\Theta, \tag{23}$$

$$\partial_t\omega + \frac{4\pi}{\Gamma}\{\Psi,\omega\} = Pr\nabla'^2\omega - PrRa\frac{2\pi}{\Gamma}\partial_x\Theta. \tag{24}$$

with all fields being periodic in the x direction and having 0 boundary conditions at $z = \pm 1$. The 0 boundary conditions on Ψ are what makes this a free-slip problem.

3 Stability of solutions

3.1 Linearization about the static state

In order to simplify computation and avoid convergence to a trivial solution, it is often useful to consider perturbations to background fields instead of the entire field. Here, we introduce the background and perturbed fields and then linearize the Boussinesq equations to determine where stable and unstable solutions lie and find the transition between them.

Consider the case where the fluid is motionless and the temperature T_0 only depends linearly on z. This means that $\Psi_0 = 0$ and gives a differential equation to solve for T_0. Specifying that $T_0(-1) = 1$ and $T_0(1) = -1$ we obtain a boundary value problem to solve for T_0.

$$\frac{d^2T_0}{dz^2} = 0,\ T_0(-1) = 1,\ T_0(1) = -1. \tag{25}$$

The form of T_0 in (22) satisfies all of these conditions, so we will have $T_0(z) = -z$. Let Θ be a perturbation to $T_0(z)$ and let Ψ be a perturbation to $\Psi_0 = 0$. Making use of (23) and (24) and setting time derivatives to zero and dropping the nonlinear terms, we obtain the equations

$$-\frac{2\pi}{\Gamma}\partial_x\Psi = \nabla'^2\Theta, \tag{26}$$

$$\nabla'^4\Psi = -Ra\frac{2\pi}{\Gamma}\partial_x\Theta. \tag{27}$$

Taking $\frac{2\pi}{\Gamma}\partial_x(26)$ and $\nabla'^2(27)$ and using the fact that these derivatives commute, we find

$$-\frac{4\pi^2}{\Gamma^2}\partial_x^2\Psi = \frac{2\pi}{\Gamma}\nabla'^2\partial_x\Theta, \tag{28}$$

$$\nabla'^6\Psi = -Ra\frac{2\pi}{\Gamma}\nabla'^2\partial_x\Theta. \tag{29}$$

These equations can be combined to find a differential equation for Ψ,

$$\nabla'^6\Psi = Ra\frac{4\pi^2}{\Gamma^2}\partial_x^2\Psi. \tag{30}$$

3.2 Linear instability of the static state

Since we must solve a sixth order equation, we need six boundary conditions in total on Ψ and its derivatives. We want the vertical fluid velocity to be zero at the boundaries. Since the vertical fluid velocity $w = \partial_x\Psi$ we can find the first two boundary conditions by setting $w = 0$ at the boundaries. The next two arise as a result of (5), and since Θ is a constantalong $z = \pm1$, $\partial_x\Theta(z = \pm1) = 0$, which gives the last boundary conditions from (27):

$$\partial_x\Psi(z = \pm1) = 0, \tag{31}$$

$$\nabla'^2\partial_x\Psi(z = \pm1) = 0, \tag{32}$$

$$\nabla'^4\partial_x\Psi(z = \pm1) = 0. \tag{33}$$

Horizontal periodicity allows us to seek solutions of the form $\Psi(x, z) = \hat{\Psi}(z)\sin x$. Under this ansatz, derivatives of Ψ taken with respect to x do not affect its z dependence. Since $\partial_x^2\Psi = -\Psi$,

the operator $(\frac{2\pi}{\Gamma})^2\partial_x^2 = -(\frac{2\pi}{\Gamma})^2$ and the boundary conditions above can be rewritten as

$$\hat{\Psi}(z = \pm 1) = 0, \tag{34}$$

$$\partial_z^2\hat{\Psi}(z = \pm 1) = 0, \tag{35}$$

$$\partial_z^4\hat{\Psi}(z = \pm 1) = 0. \tag{36}$$

These boundary conditions are satisfied by $\hat{\Psi}_n(z) = \cos(n - \frac{1}{2})\pi z$ for integers n. Since we are interested in solutions with only one layer of convection cells in the vertical direction, we choose $n = 1$. Substituting this in to (30) gives

$$(\pi^2 + (\frac{2\pi}{\Gamma})^2)^3 = Ra\frac{4\pi^2}{\Gamma^2}. \tag{37}$$

Rearranging this equation we find an expression for Ra as a function of Γ^2,

$$Ra(\Gamma^2) = \frac{\Gamma^2}{4\pi^2}(\pi^2 + (\frac{2\pi}{\Gamma})^2)^3. \tag{38}$$

The critical value Γ^2_{cr} that minimizes the above function gives the minimum Rayleigh number Ra_{cr} where unstable solutions first appear. Basic calculus gives

$$\Gamma^2_{cr} = 8, \tag{39}$$

$$Ra_{cr} = Ra(\Gamma^2_{cr}) = \frac{27}{4}\pi^4. \tag{40}$$

The stable and unstable regions in the (k, Ra) plane, where $k = \frac{2\pi}{\Gamma}$ is the horizontal wavenumber, are shown in figure 1. The minimum of the curve corresponds to the critical value Ra_{cr}.

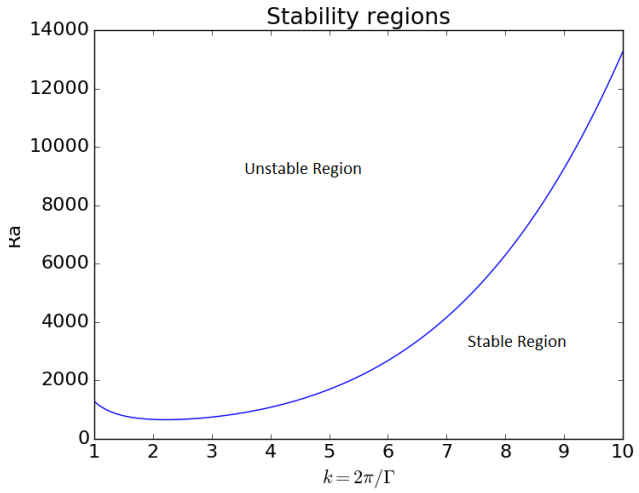

Figure 1: $Ra_{cr}(k)$ showing a minimum at Ra_{cr}, where unstable solutions are first found.

Given our chosen initial conditions, solutions in this unstable region will be pairs of convecting rolls which can be seen through a plot of the level sets of $\Psi(x, z)$ in figure 2. The magnitude of $\Psi(x, z)$ corresponds to the speed of the fluid at that point, and the fluid moves at the same speed at all points on a given level set of $\Psi(x, z)$. Since we are working with periodic boundaries, we can see in the following plots that the fluid rises at $x = (2n + 1)\pi$ and falls at $x = 2n\pi$, where n is an integer.

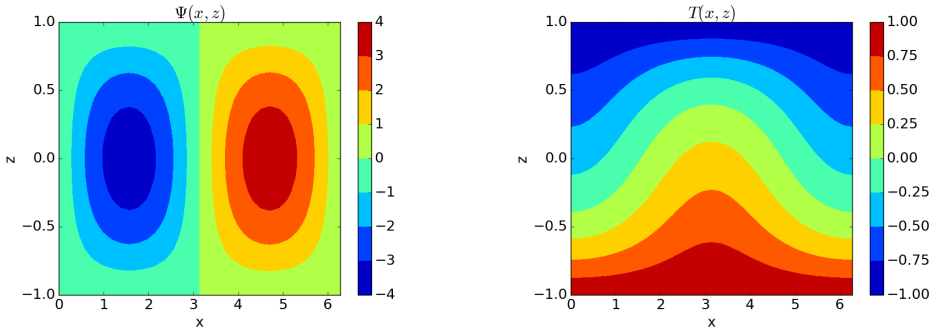

Figure 2: $\Psi(x,z)$ and $T(x,z)$ at $Ra = 10^3$.

4 Numerical computation of steady states

In order to find the steady state temperature field, we need to solve (23)–(24) numerically with $\partial_t T = 0$, which have done using Newton's method. Given a system of equations $\mathbf{F}(\mathbf{x}) = 0$, Newton's method searches for the solution $\mathbf{x}$ using the iterative process:

$$J_F \mathbf{\Delta x_n} + \mathbf{F}(\mathbf{x_n}) = 0, \ \mathbf{x_{n+1}} = \mathbf{x_n} + \mathbf{\Delta x}, \tag{41}$$

where $\mathbf{x_n}$ is a vector of state variables with components x_j and J_F is the Jacobian matrix of the system defined by $J_{ij} = \frac{\partial F_i}{\partial x_j}$, where F_i is the i^{th} component of $\mathbf{F}$. We will look to use Newton's Method to solve for Ψ and Θ simultaneously.

To calculate the temperature distribution we make use of (23) and enforce the boundary conditions $\Theta(x, \pm 1) = 0, \ \Theta(0, z) = \Theta(2\pi, z)$. We begin by constructing a discretized $N \times N$ domain with uniform discretization in the x direction and Chebyshev discretization in the z direction. In order to write (23) in a form that allows us to use Newton's method, we construct differentiation matrices for the x and z directions using spectral methods. Since the z direction is treated with Chebyshev spacing and the boundary conditions in x are periodic, we use a Chebyshev differentiation matrix in z and a Fourier differentiation matrix in x. Let Dz be the Chebyshev differentiation matrix and Dx be the Fourier differentiation matrix, each with appropriate scaling as described by (19). In order to ensure that we respect boundary conditions, the differentiation matrices are stripped of their first and last rows, leaving us with two $N \times N$ differentiation matrices.

To solve (23) for Θ, we select a stream function $\Psi(x,z)$ that respects the boundary conditions on $\Psi(x,z)$ and create an $(N+2) \times N$ array of values of Ψ on the discretized spatial domain, which is then stripped of its first and last rows and reshaped in to a vector $\mathbf{\Psi}$ with length N^2. To differentiate this, we use the Kronecker product $\otimes$ to create new $N^2 \times N^2$ differentiation matrices Dx_{in} and Dz_{in}:

$$Dx_{in} = I_N \otimes Dx, \tag{42}$$

$$Dz_{in} = Dz \otimes I_N, \tag{43}$$

where I_N is the $N \times N$ identity matrix. The second derivatives are given by Dx_{in}^2 and Dz_{in}^2, allowing the Laplacian and Poisson bracket to be written as

$$\nabla^2 = Dx_{in}^2 + Dz_{in}^2, \tag{44}$$

$$\{\mathbf{\Psi}, \mathbf{\Theta}\} = Dx_{in}\mathbf{\Psi} \circ Dz_{in}\mathbf{\Theta} - Dx_{in}\mathbf{\Theta} \circ Dz_{in}\mathbf{\Psi}, \tag{45}$$

where $\circ$ represents the Hadamard product.

4.1 Reformulating the equations

We can then write (23) and (24) as an algebraic system using the Hadamard product. Since Ψ and ω are related in a simple manner by (5), we can replace any reference to ω by $-\nabla^2\Psi$ and reduce the system of equations with three variables to a system with two variables. These new equations take the form

$$\mathbf{F}(\mathbf{\Theta}) = Dx_{in}\mathbf{\Psi} \circ Dz_{in}\mathbf{\Theta} - Dx_{in}\mathbf{\Theta} \circ Dz_{in}\mathbf{\Psi} - Dx_{in}\mathbf{\Psi} - \nabla^2\mathbf{\Theta} = 0, \tag{46}$$

$$\mathbf{F}(\mathbf{\Psi}) = -Dx_{in}\mathbf{\Psi} \circ Dz_{in}\nabla^{\mathbf{2}}\mathbf{\Psi} + Dz_{in}\mathbf{\Psi} \circ Dx_{in}\nabla^{\mathbf{2}}\mathbf{\Psi} + Pr\nabla^4\mathbf{\Psi} + PrRaDx_{in}\mathbf{\Theta} = 0 \tag{47}$$

Now, we can apply the method used in [9], where the system of equations is solved via Newton's method with a single Jacobian matrix. To do this, we define a new vector $\mathbf{v}(\mathbf{\Theta}, \mathbf{\Psi})$ and a new vector function $\mathbf{G}(\mathbf{v})$, each with length $2N^2$. These new vectors will be defined so that the first N^2 entries are $\mathbf{\Theta}_i$ and $\mathbf{F}(\mathbf{\Theta})_i$ respectively, and the last N^2 entries are $\mathbf{\Psi}_i$ and $\mathbf{F}(\mathbf{\Psi})_i$. Using this, we can define a Jacobian using $\mathbf{G}$ and $\mathbf{v}$, allowing us to solve for both $\mathbf{\Theta}$ and $\mathbf{\Psi}$ at the same time.

4.2 Exploiting symmetry

The Fourier differentiation matrices work by assuming only that the functions they are applied to are 2π–periodic and says nothing about forced symmetry over the interval. However, all three of Θ, Ψ, and ω have some sort of symmetry on the interval $[0, 2\pi)$ that we can exploit to make our differentiation matrices one quarter of the size they would be otherwise, allowing for a huge increase in computational speed.

Due to our periodic boundary conditions and the basis we've chosen for them, the variables Θ and Ψ are even and odd about $x = \pi$ respectively, and ω inherits the same symmetry as Ψ due to how it has been defined. This allows us to halve the set of basis functions for each of these variables by ignoring those with the opposite symmetry over π, giving us two matrices meant for differentiation of even and odd functions. Since the derivative of a function has the opposite symmetry of the function, we also need two different matrices for the second derivatives. A more complete discussion can be found in [7].

4.3 Changing Ra

Using the methods described in the previous parts of this section, we are able to write code to solve the Boussinesq equations and calculate Nu at increasing values of Ra, which we have chosen to be logarithmically spaced. We begin our iteration at $Ra = 10^3$ with initial conditions for $\Psi(x, z) = \sin x \cos \frac{\pi}{2} z$ and $\Theta(x, z) = \cos x \cos \frac{\pi}{2} z$ and combine the values for both of these variables in to a single vector $\mathbf{v}$ as described in section 4.1. Using these, we iterate Newton's method until $||\mathbf{v}||_\infty < \epsilon(N)$ a prescribed tolerance, where the argument is used to indicate that this value of ϵ increases as the spatial resolution increases to limit effects from numerical noise which can be amplified at high resolutions. We then use these converged values of $\mathbf{v}$ to find good initial conditions for use at the next value of Ra.

In order to accelerate convergence at high values of Ra, we store the previous values of $\mathbf{v}$ at every point in the spatial domain. We can then use these as well as the Rayleigh number they were generated at to allow for extrapolation of $\mathbf{v}$ to the next Rayleigh number via cubic splines. We can then use this extrapolated value of $\mathbf{v}$ as a slightly more accurate initial guess than if we had just used the value of $\mathbf{v}$ at the previous value of Ra. This approach saves valuable time when the resolution gets finer and calculations become very computationally expensive.

4.4 Changing resolution

As Ra increases, we require finer spatial resolution to give accurate solutions from which we can calculate Nu. We determine which resolution is sufficient at each value of Ra by comparing calculations of Nu at several resolutions. Once we are convinced that increasing resolution will not affect the calculation, we settle on that resolution. In the cases where the values of Nu are close together, we say that the calculations are well-converged. This dependence on the resolution is demonstrated in table 1, where for lower values of Ra all pictured resolutions will agree, but their separation becomes larger as Ra increases.

Dependence of Nu on resolution N				
N	$Ra = 10^3$	$Ra = 10^4$	$Ra = 10^5$	$Ra = 10^6$
64	1.7385935	5.086978	11.620777	28.645699
80	1.7385935	5.086978	11.618579	26.610504
112	1.7385935	5.086942	11.618436	25.778404
128	1.7385935	5.086902	11.618335	25.713831
160	1.7385935	5.086748	11.618075	25.686192
176	1.7385935	5.086748	11.618076	25.684132

Table 1: The dependence of Nu on resolution. Note how increasing Ra creates a need for higher resolution to get well-converged solutions.

In order to keep solutions well-converged, we update the resolution whenever $\log_{10}(Ra)$ is an integer or half-integer, or whenever the slope between the last and second to last point in the $(\log_{10}(Ra), \log_{10}(Nu))$ plane is larger than that between the third to last and second to last points. In the event that the resoluton needs to be increased, we can apply Fourier and Chebyshev transforms to both $\Psi(x, z)$ and $\Theta(x, z)$ to give a spectrally accurate interpolation on to the finer grid by padding the end of the transformed frequencies with an appropriate number of zeros and then applying the inverse transform. In order to allow for the extrapolation described in section 4.3 to work with updated resolution, we apply the same method to the stored values of $\mathbf{\Psi}$ and $\mathbf{\Theta}$ at the previous four values of the Rayleigh number. Once we have done this, we update all differentiation matrices and continue at the new resolution.

5 Calculating the Nusselt number

Once we have found the steady solution to the Boussinesq equations at a given Ra and Pr, we can use those solutions to find the Nusselt number, or the ratio of total heat transfer to conductive heat transfer. There are several equivalent expressions for the Nusselt number (let $\langle . \rangle$ denote a volume average and $\bar{.}$ denote a horizontal average):

$$Nu = 1 + \langle wT \rangle, \tag{48}$$

$$Nu = -\frac{d}{dz}\bar{T}|_{z=1}, \tag{49}$$

$$Nu = \langle |\nabla T|^2 \rangle, \tag{50}$$

$$Nu = 1 + \frac{1}{Ra}\langle |\nabla u|^2 \rangle. \tag{51}$$

In terms of Θ and Ψ, where $T = T_0 + \Theta$ and $w = \frac{d}{dx}\Psi$, we can rewrite (48) as

$$Nu = 1 + \langle(\Theta - z)\frac{d}{dx}\Psi\rangle = 1 + \langle\Theta\frac{d}{dx}\Psi\rangle - \langle z\frac{d}{dx}\Psi\rangle. \tag{52}$$

Letting Ω be the spatial domain $[0, 2\pi) \times [-1, 1]$, the volume average of a function $f(x, z)$ defined on Ω is

$$\langle f(x,z)\rangle = \frac{1}{4\pi}\int_\Omega f(x,z)d\Omega. \tag{53}$$

Using this, we can rewrite (52) as

$$Nu = 1 + \frac{1}{4\pi}(\int_\Omega \Theta\frac{d\Psi}{dx}d\Omega - \int_\Omega z\frac{d\Psi}{dx}d\Omega). \tag{54}$$

Since z is constant with respect to x and $d\Omega = dxdz$ the second integral can be written as $\int_{-1}^{1} z(\int_0^{2\pi}\frac{d\Psi}{dx}dx)dz = \int_{-1}^{1} z(\Psi(2\pi, z) - \Psi(0, z))dz = 0$ since boundary conditions force $\Psi(0, z) = \Psi(2\pi, z)$. We can now rewrite (54) as

$$Nu = 1 + \frac{1}{4\pi}(\int_\Omega \Theta\frac{d\Psi}{dx}d\Omega) = 1 + \langle\frac{d\Psi}{dx}\Theta\rangle. \tag{55}$$

After re-scaling to fit our domain, this is equivalent to

$$Nu = 1 + \frac{2\pi}{\Gamma}\langle\frac{d\Psi}{dx}\Theta\rangle. \tag{56}$$

Likewise, we can rewrite (49) as

$$Nu = -\frac{d}{dz}\overline{(\Theta - z)}|_{z=1}. \tag{57}$$

Taking the derivative, we find that this is equivalent to

$$Nu = -\overline{(\frac{d}{dz}\Theta - 1)|_{z=1}}. \tag{58}$$

Re-scaling to our domain we find that this is equal to

$$Nu = -\overline{(2\frac{d}{dz}\Theta - 1)|_{z=1}}. \tag{59}$$

By again letting $T = \Theta - z$ in (50) we find

$$Nu = \langle|\nabla(\Theta - z)|^2\rangle = \langle(\frac{d}{dx}(\Theta - z))^2 + (\frac{d}{dz}(\Theta - z))^2\rangle. \tag{60}$$

Taking the derivatives and rescaling, this becomes

$$Nu = \langle(\frac{2\pi}{\Gamma}\frac{d}{dx}\Theta)^2 + (2\frac{d}{dz}\Theta - 1)^2\rangle. \tag{61}$$

Noting that $\langle(2\frac{d}{dz}\Theta - 1)^2\rangle = \langle 1 - 2\frac{d}{dz}\Theta + 4(\frac{d}{dz}\Theta)^2\rangle = \langle 1\rangle - 2\langle\frac{d}{dz}\Theta\rangle + \langle(2\frac{d}{dz}\Theta)^2\rangle$ we can simplify this further. From (53) we can calculate $\langle\frac{d}{dz}\Theta\rangle = \int_0^{2\pi}\int_{-1}^{1}(\frac{d}{dz}\Theta)dzdx = \int_0^{2\pi}(\Theta(1) - \Theta(-1))dx = 0$ because $\Theta(\pm 1) = 0$ from boundary conditions. We can use this calculation to simplify (61) even further:

$$Nu = 1 + \langle(\frac{2\pi}{\Gamma}\frac{d}{dx}\Theta)^2\rangle + \langle(2\frac{d}{dz}\Theta)^2\rangle. \tag{62}$$

Lastly, we can write the vector $\mathbf{u}$ in (51) in terms of its components $(u, w) = (-\partial_z \Psi, \partial_x \Psi)$, which turns the equation into one for the average of the squared norm of $\nabla(-\partial_z \mathbf{\Psi}, \partial_x \mathbf{\Psi})$, which is the sum of squared entries of the matrix.

$$Nu = 1 + \frac{1}{Ra}\langle 2(\frac{d^2}{dxdz}\Psi)^2 + (\frac{d^2}{dz^2}\Psi)^2 + (\frac{d^2}{dx^2}\Psi)^2\rangle. \tag{63}$$

Re-scaling, we see that this is equal to

$$Nu = 1 + \frac{1}{Ra}\langle 2(\frac{\pi}{\Gamma}\frac{d^2}{dxdz}\Psi)^2 + (\frac{1}{4}\frac{d^2}{dz^2}\Psi)^2 + ((\frac{2\pi}{\Gamma})^2\frac{d^2}{dx^2}\Psi)^2\rangle. \tag{64}$$

It can be shown that the first term averages to 0, so this becomes

$$Nu = 1 + \frac{1}{Ra}\langle \nabla'^2 \Psi\rangle. \tag{65}$$

So the new expressions for calculation of Nu are given by (56), (59), (62), and (65). These values are calculated at each each value of Ra and their average is taken to lessen the effect of small numerical error in any one of the calculations. This average is what is used in all calculations of Nu.

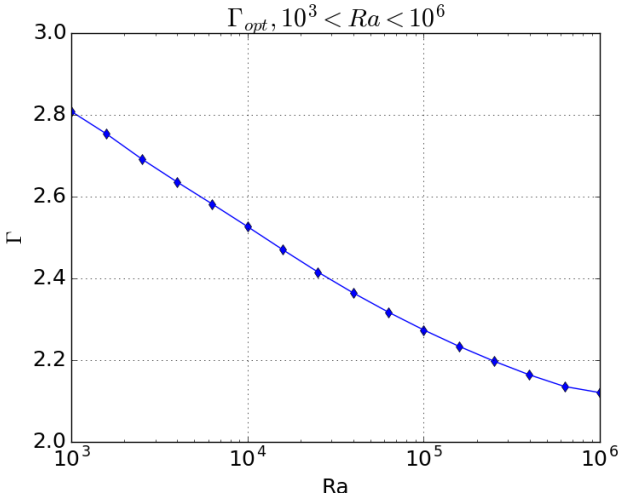

Figure 3: $\Gamma_{opt}(Ra)$

6 Optimization over Γ

In order to allow the Nusselt number to increase as quickly as possible, we calculate the optimal aspect ratio for the domain at each Ra.To calculate Γ_{opt}, we select evenly spaced points from an interval as test values for Γ and run the routine stepping through Ra at each of the pre-selected Γ. Upon completion of the calculation of $Nu(Ra;\Gamma)$ at each Γ, we arrange the results to group the various calculated values of $Nu(Ra;\Gamma)$ together for each fixed Ra. The curves of $Nu(\Gamma)$ at fixed Ra have a single local maximum, which allowed us to use convex optimization routines to calculate $\Gamma_{opt}(Ra)$ at each Ra and use that information to calculate $Nu(Ra;\Gamma_{opt})$. In [10], at $Pr = 1$ they find extra curvature in the plot of Nu vs Γ beyond a single local maximum, however it occurs at higher wavenumber than investigated here so there may still be similar behavior to find. A plot

of $\Gamma_{opt}(Ra)$ shown in figure 3. These results are similar to what was found in [1], where Γ_{opt} was found to vary little over large changes in Ra. We observe a change from $\Gamma_{opt} \approx 2.81$ at $Ra = 10^3$ to $\Gamma_{opt} \approx 2.12$ at $Ra = 10^6$, a small change for such a large change in Ra. We can see this change in Γ_{opt} for several Ra in figure 4.

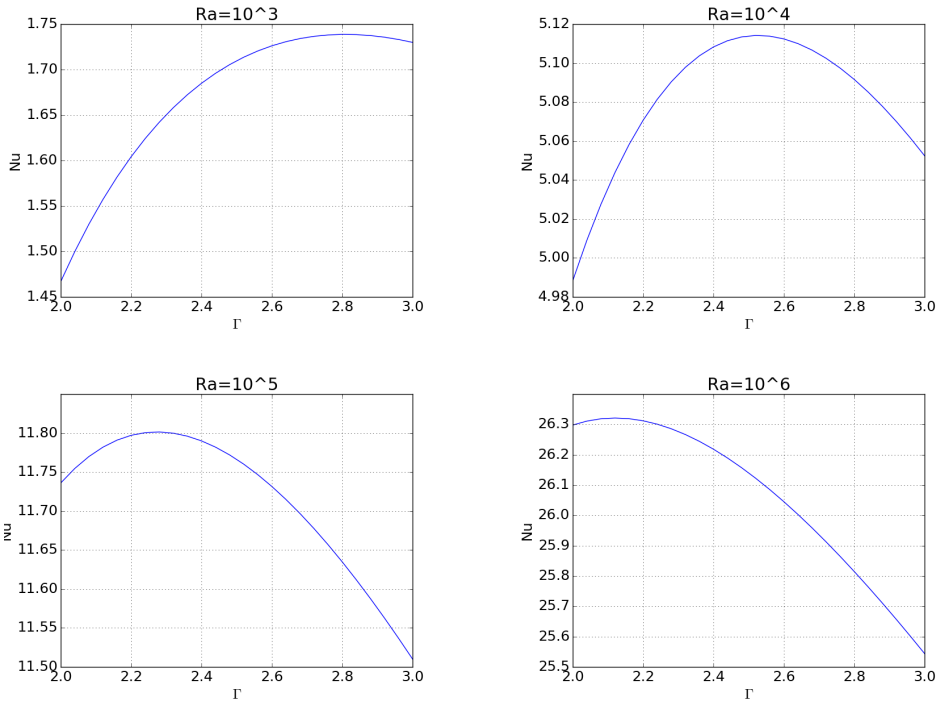

Figure 4: $Nu(\Gamma)$ at $Ra = 10^3, 10^4, 10^5, 10^6$ showing single peaks at Γ_{opt}.

Work in [3] shows that, in the case where Γ is fixed and Pr is of moderate size, the optimal wave number $k \approx \pi$, which means that Γ_{opt} should approach 2 as $Ra \to \infty$. The curvature near $Ra = 10^6$ in figure 3 suggests that this may still be possible, but further investigation would be needed to conclude anything. It is interesting to note that in the no-slip case the optimal aspect ratio is described by a power law [2], but that may not be the case here.

7 Results

In [4] it was shown that the non-optimized case yields $Nu(Ra;\Gamma) \sim Ra^{1/3}$ in the limit $Ra \to \infty$, and work done in [6] has proven that $Nu(Ra;\Gamma)$ cannot scale faster than $Ra^{5/12}$. By optimizing over Γ we hope to force the power law exponent as high as possible.

Since the difference between the optimized and non-optimized calculations is small, we can get a better view of the situation if we look at a plot of the percent difference in Nu between the two cases normalized by the non-optimized case. This is shown in figure 5. The difference between the calculated values of Nu starts off around 10^{-5}, but as $Ra \to \infty$ the difference increases and is close to 1 at $Ra = 10^6$. We see that the percent difference is increasing throughout the interval $10^3 < Ra < 10^6$.

So, while it doesn't seem that the optimization has changed the scaling exponent, it is possible that the prefactor in the power law relation has changed, that is, the value of C in the expression $Nu \sim CRa^{1/3}$. In [3], Chini and Cox calculate the value of C to be approximately 0.2629. If, as we

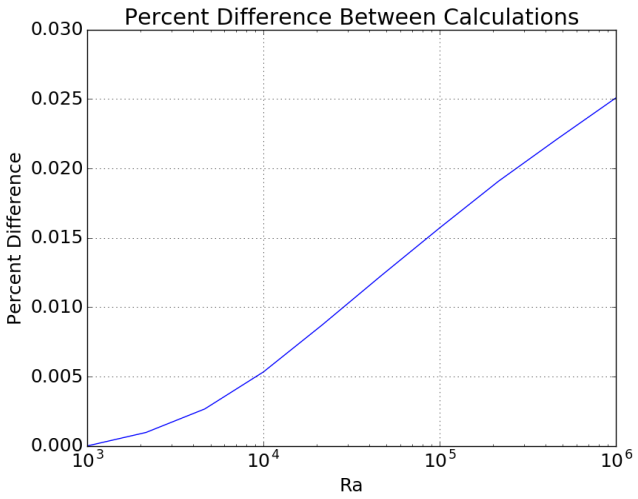

Figure 5: log-linear plot of the difference between the optimized and non-optimized cases

suspect, $Nu(Ra;\Gamma_{opt})$ is asymptotic to $C_{opt}Ra^{1/3}$ for some C_{opt} as $Ra \to \infty$, then as $Ra \to \infty$ we expect that the ratio $Nu(Ra;\Gamma_{opt})/Ra^{1/3} \to C_{opt}$. Since $Nu(Ra,\Gamma_{opt}) < C_{opt}Ra^{1/3}$ for all values of Ra, we expect to be able to use this ratio to obtain a lower estimate on C_{opt}.

From the data used in figure 6, we see that in the non-optimized case $C > 0.257$, which agrees with the number provided by Chini and Cox. However, in the optimized case the lower estimate on the value of C has already passed the value given by Chini and Cox, with the data from figure 6 giving a lower estimate of $C_{opt} > 0.263$. So it appears that all the difference in scaling is made by the change in the prefactor. In the nonoptimized case, there is a 2.4% increase from this lower estimate of 0.257 to Chini and Cox's value. If we assume that the optimized case scales similarly, then this gives a value of $C_{opt} \approx 0.270$, so $Nu_\infty(Ra) \approx 0.270Ra^{1/3}$.

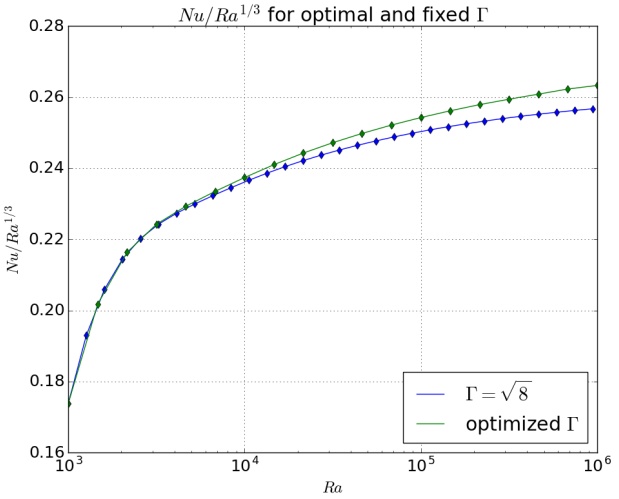

Figure 6: $Nu/Ra^{1/3}$ for optimal and fixed Γ

This calculated prefactor makes for a convincing asymptotic limit. The figure below shows the scaling of the calculated value of $Nu(Ra)$ with the asymptotic limit, showing that it approaches the limit as Ra increases like we expect it to.

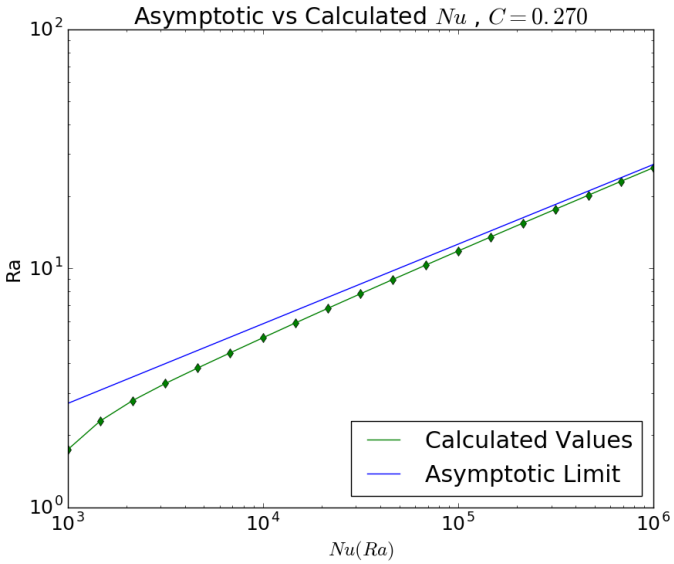

Figure 7: Calculated value of $Nu(Ra)$ approaching $Nu_\infty = 0.270 Ra^{1/3}$

For Rayleigh–Bénard convection between free-slip boundaries with $Pr = 1$, we have found that optimizing the aspect ratio of steady convection cells does not change the power-law scaling of the Nusselt number. At asymptotically large Rayleigh numbers, the Nusselt number grows with the same $Ra^{1/3}$ scaling reported for a fixed aspect ratio in [3], although the prefactor is larger in the optimized case. These findings are in contrast to the case of no-slip boundaries, where optimizing the aspect ratio does raise the exponent of the power-law scaling of $Nu(Ra)$, and the optimal aspect ratio decreases much more quickly as Ra is raised [2, 10]. More work is needed to understand the physical mechanism that creates this difference between the free-slip and no-slip cases. In ongoing computations, we are exploring how the reported results depend on the Prandtl number, which has a significant effect in the no-slip case [10]. In doing so, we hope to complete the characterization of steady states in Rayleigh's model that he began a century ago.

References

[1] Andre Souza and Charles R. Doering *MLB Extended Abstract: Optimizing Heat Transport in Boussinesq Convection*

[2] Fabian Waleffe, Anakewit Boonkasame, and Leslie M. Smith, *Heat transport by coherent Rayleigh–Bénard convection* Physics of Fluids **27**, 051702 (2015)

[3] Gregory P. Chini and Stephen M. Cox, *Large Rayleigh number thermal convection: Heat flux predictions and strongly nonlinear solutions* Physics of Fluids **21**, 083603 (2009)

[4] Grossman, S. and Lohse, D. *Scaling in thermal convection: a unifying theory.* J. Fluid Mech. 407, 27 (2000).

[5] J. R. A. Pearson, *On convection cells induced by surface tension* Journal of Fluid Mechanics, 4(5), pp. 489500. (1958)

[6] Jared P. Whitehead and Charles R. Doering *Ultimate State of Two-Dimensional Rayleigh–Bé nard Convection between Free-Slip Fixed-Temperature Boundaries* Physical Review Letters **106**, 244501 (2011)

[7] John P. Boyd, *Fourier and Spectral Methods Second Edition, 2nd ed.* Dover, 2000

[8] Lord Rayleigh, *On Convection Currents in a Horizontal Layer of Fluid, when the Higher Temperature is on the Under Side* The London, Edinburgh, and Dublin Philosophical Magazine and Journal of Science, S. 6 Vol 32 No. 192 (1916)

[9] Pedram Hassanzadeh, Gregory P. Chini, and Charles R. Doering, *Wall to Wall Optimal Transport* (2014)

[10] D. Sondak, L.M. Smith, and F. Waleffe, *Optimal Heat Transport Solutions for Rayleigh–Bénard Convection* (2015)